The FASEB Journal article fj.14-269522. Published online May 14, 2015.

Nucleophosmin contains amyloidogenic regions that are able to form toxic aggregates under physiological conditions

Concetta Di Natale,*[,1,2] Pasqualina Liana Scognamiglio,*[,†,1,2] Roberta Cascella,[‡] Cristina Cecchi,[‡] Anna Russo,*[,3] Marilisa Leone,[†,§] Amanda Penco,[¶] Annalisa Relini,[¶] Luca Federici,[‖] Adele Di Matteo,[#] Fabrizio Chiti,[‡] Luigi Vitagliano,[†,§] and Daniela Marasco*[,†,4]

*Department of Pharmacy, Diagnostica e Farmaceutica Molecolari-Società Cooperativa a Responsabilità Limitata, [†]Centro Interuniversitario di Ricerca sui Peptidi Bioattivi, University of Naples "Federico II," Naples, Italy; [‡]Section of Biochemistry, Department of Biomedical Experimental and Clinical Sciences "Mario Serio," University of Florence, Florence, Italy; [§]Institute of Biostructures and Bioimaging, Consiglio Nazionale delle Ricerche, Naples, Italy; [¶]Department of Physics, University of Genoa, Genoa, Italy; [‖]Department of Medical, Oral, and Biotechnological Sciences, University of Chieti "G. d'Annunzio," Chieti, Italy; and [#]Institute of Molecular Biology and Pathology, Consiglio Nazionale delle Ricerche, Rome, Italy

ABSTRACT **Nucleophosmin (NPM)-1 is a multifunctional protein involved in a variety of biologic processes and has been implicated in the pathogenesis of several human malignancies. To gain insight into the role of isolated fragments in NPM1 activities, we dissected the C-terminal domain (CTD) into its helical fragments. In this study, we observed the unexpected structural behavior of the peptide fragment corresponding to helix (H) 2 (residues 264–277). This peptide has a strong tendency to form amyloidlike assemblies endowed with fibrillar morphology and β-sheet structure, under physiologic conditions, as shown by circular dichroism, thioflavin T, and Congo red binding assays; dynamic light scattering; and atomic force microscopy. The aggregates are also toxic to neuroblastoma cells, as determined using 3-(4;5-dimethylthiazol-2-yl)-2,5-diphenyltetrazolium bromide reduction and Ca^{2+} influx assays. We also found that the extension of the H2 sequence beyond its N terminus, comprising the connecting loop with H1, delayed aggregation and its associated cytotoxicity, suggesting that contiguous regions of H2 have a protective role in preventing aggregation. Our findings and those in the literature suggest that the helical structures present in the CTD are important in preventing harmful aggregation. These findings could elucidate the pathogenesis of acute myeloid leukemia (AML) caused by NPM1 mutants. Because the CTD is not properly folded in these mutants, we hypothesize that the aggregation propensity of this NPM1 region is involved in the pathogenesis of AML. Preliminary assays on NPM1-Cter-MutA, the most frequent AML-CTD mutation, revealed its significant propensity for aggregation. Thus, the aggregation phenomena should be seriously considered in studies aimed at unveiling the molecular mechanisms of this pathology.—Di Natale, C., Scognamiglio, P. L., Cascella, R., Cecchi, C., Russo, A., Leone, M., Penco, A., Relini, A., Federici, L., Di Matteo, A., Chiti, F., Vitagliano, L., Marasco, D. Nucleophosmin contains amyloidogenic regions that are able to form toxic aggregates under physiological conditions. *FASEB J.* 29, 000–000 (2015). www.fasebj.org**

Key Words: β aggregate · acute myeloid leukemia · circular dichroism spectroscopy · AFM · MTT assay

NUCLEOPHOSMIN (NPM)-1 (ALSO KNOWN AS B23, No38, and numatrin) is an abundant multifunctional protein, initially identified as a nuclear phosphoprotein, that constantly shuttles between the nucleus and cytoplasm. It is present in high quantities in the granular region of nucleoli (1, 2). Three distinct isoforms have been reported to be expressed in human cells: B23.1, the longest and the most abundant (294 residues), is also the best characterized isoform; B23.2 and B23.3 are splicing variants that lack the C-terminal 35 aa and a 29 aa segment (residues 195–223) in

Abbreviations: AFM, atomic force microscopy; AML, acute myeloid leukemia; ARF, alternate reading frame; CD, circular dichroism; CR, Congo red; CSSP, contact-dependent secondary structure propensity; CTD, C-terminal domain; DLS, dynamic light scattering; DMF, *N,N*-dimethylformamide; Fmoc, fluorenylmethoxycarbonyl; H, helix (with numbers 1–3);

(*continued on next page*)

[1] These authors contributed equally to this work.

[2] Current affiliation: Center for Advanced Biomaterials for Healthcare, Centro Interdipartimentale di Ricerca sui Biomateriali, Istituto Italiano di Tecnologia, Naples, Italy.

[3] Current affiliation: Department of Medical Biotechnology, Policlinico Le Scotte, University of Siena, Siena, Italy.

[4] Correspondence: Department of Pharmacy, University "Federico II," Via Mezzocannone, 16, 80134, Naples, Italy. E-mail: daniela.marasco@unina.it

doi: 10.1096/fj.14-269522

This article includes supplemental data. Please visit *http://www.fasebj.org* to obtain this information.

the basic region, respectively (3). Structural characterizations of B23.1 have shown that it is endowed with a modular structure (Supplemental Fig. S1). The N-terminal domain, also called the oligomerization domain, extends for approximately 100 residues and displays an 8-stranded β-barrel fold. Five N-terminal domains oligomerize to form a crown-shaped homopentamer. Two or more of these pentamers may associate to form decamers or higher oligomeric species (4). A recent study has shown that this domain exhibits structural polymorphism by populating conformational states ranging from a highly ordered and folded pentamer to a highly disordered monomer and that the monomer-pentamer equilibrium is modulated by post-translational modifications, ionic strength, and protein binding (5).

The central portion of NPM1 is characterized by the presence of 2 acidic domains (residues 119–133 and 161–188) and a basic region (residues 198–239). These domains although unstructured, are crucial for the DNA/RNA recognition mechanism (6, 7). The C-terminal domain (CTD) encompasses residues 241–294 (**Fig. 1**). It forms a globular structure consisting of a 3-helix bundle, and for this reason it is also called the 3-helix-bundle domain (8). Atomistic NMR investigations have shown that 3 helices span residues 243–259 (H1), 264–277 (H2), and 280–294 H3). Secondary structure prediction analysis indicates that the helical regions of the CTD are endowed with a strong intrinsic propensity to adopt this particular type of secondary structure (Supplemental Fig. S2*A*).

NPM1 has been the subject of several biophysical characterizations focused on the stability of the full-length protein or of its isolated domains. These analyses have shown that the N-terminal domain is endowed with a thermal and chemical stability, with no unfolding observed when increasing the temperature to 90°C or adding urea; by contrast, the CTD has been found to have a markedly lower stability (9). Investigations of the CTD have provided a detailed characterization of the complete folding pathway of this domain (10–12). It folds *via* a compact transition state characterized by an extended nucleus. Furthermore, these studies have shown that the unfolded state is characterized by malleable residual secondary structure at the interface between the second and third helices and that a mutual stabilization of the N- and the C-terminal-folded domain occurs through a central intrinsically disordered region (9–11, 13).

NPM1 belongs to the nucleophosmin/nucleoplasmin family of proteins (14) and associates with DNA and RNA, processes RNA, prevents misfolding and aggregation of target proteins as a molecular chaperone, and mediates chromatin assembly and disassembly as a histone chaperone (15, 16). The N-terminal domain is responsible for its chaperone activities, whereas the C-terminal region binds nucleic acids. The presence of several nuclear and nucleolar import/export signals in the NPM1 sequence indicates the prominent role of NPM1 in nuclear or nucleolar protein import; indeed, it is involved in several biologic processes, such as ribosome biogenesis, tumor suppression, and nucleolar stress response (17, 18). This protein has been found to be overexpressed in tumors of different histologic origin, including gastric, ovarian, bladder, and prostate carcinomas and in various hematologic malignancies (19–22). NPM1 also has been implicated in the apoptotic response to stress and oncogenic stimuli (such as DNA damage and hypoxia) (23) and can modulate the activity and stability of crucial tumor-suppressor proteins such as p53 (24). Loss of NPM1 function leads to the destabilization and functional impairment of the alternate reading frame (ARF) tumor-suppressor pathway; thus, it acts as a positive regulator of ARF protein stability (25).

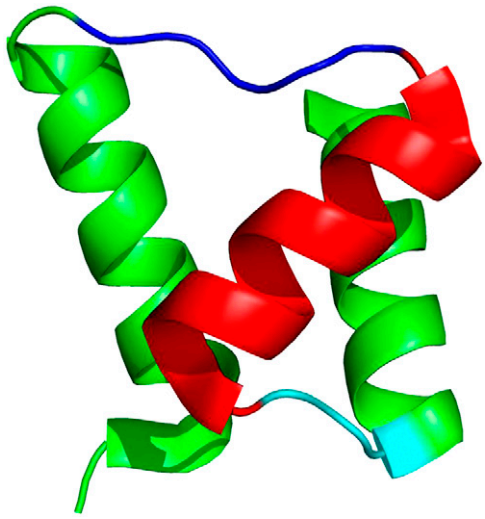

Figure 1. Ribbon structure of NPM1-CTD (residues 241–294). Fragments derived from secondary structure dissection of the 3-helix bundle are outlined in red ($H2^{264–277}$), blue (the N-terminal extension reported in sequences Nterm H2 $extended^{259–277}$ and N-, C-term H2 $extended^{259–280}$), and cyan (the C-terminal extension reported in sequences Cterm H2 $extended^{264–280}$ and N-, C-term H2 $extended^{259–280}$). Protein Data Bank code, 2VXD (8).

NPM1 has been identified as the most frequently mutated gene in acute myeloid leukemia (AML), accounting for approximately 30% of cases (24, 26–30). The most frequent human NPM1 mutations lead to variants with altered C-terminal sequences of the CTD (Supplemental Fig. S2*A*). These modifications, which involve the H3 region, lead to an unfolding of the CTD in the mutated protein (8, 11) and its accumulation in the cytoplasm, caused by the loss of nuclear localization sequences with mutations of Trp^{290} (MutE) and also of Trp^{288} (MutA) (8, 31). Indeed, most NPM1 mutations result in critical changes in the CTD, interfering with its nucleolus-cytoplasm trafficking and leading to the aberrant accumulation of the protein in the cytoplasm of the leukemic cells (thus, the term NPM cytoplasmic positive: $NPMc^+$ AML) (29). The cytoplasmic dislocation of NPM1 appears to be critical to its leukemogenic activity; thus, the increased NPM1 export into the cytoplasm affects multiple cellular pathways and may drive leukemia by either loss- or

(*continued from previous page*)

LC-MS, liquid chromatography-mass spectrometry; MTT, 3-(4; 5-dimethylthiazol-2-yl)-2, 5-diphenyltetrazolium bromide; NPM, nucleophosmin; $NPMc^+$, NPM cytoplasmic positive; pI, isoelectric point; ThT, thioflavin T; wt, wild-type

gain-of-function mechanisms. The dislocation of NPM1 in the cytoplasm causes the loss of function of this normally nuclear protein, and NPM1 interactors can be delocalized into the cytoplasm by $NPM1c^+$ and their activity significantly impaired. In addition, NPM1 mutants acquire new properties, such as the ability to interact and inhibit the cell death activity of caspase-6 and -8 in the cytoplasm (32).

Because the primary sequences of the 3 helices contained in NPM1-CTD share a high propensity to form α-helical structures (Supplemental Fig. S2*B*) (9), we dissected this domain into peptides corresponding to these helices to gain insight into their conformational behavior and their ability to interact with NPM1 biologic partners. Fragments corresponding to the H1 and H3 regions assume helical states (7) (unpublished results). In this study, the unexpected behavior of H2 is described: we serendipitously found that the fragment corresponding to the H2 region (hereafter denoted as $H2^{264–277}$) spontaneously forms stable and cytotoxic aggregates under physiologic conditions.

These aggregates appear to be amyloidlike assemblies endowed with fibrillar morphology and β-sheet structure and an ability to bind amyloid-diagnostic dyes. A preliminary characterization of the CTD bearing the most common AML mutation, NPM1-Cter-MutA, indicated a significant propensity to aggregate. The biologic implications of these findings for NPM1 functions and malfunctions are also discussed.

MATERIALS AND METHODS

Peptide synthesis

Reagents for peptide synthesis were from InBios (Naples, Italy). Solvents for peptide synthesis and HPLC analyses were from Romil (Dublin, Ireland); reversed-phase (RP) columns for peptide analysis and the liquid chromatography-mass spectrometry (LC-MS) system were from Thermo Fisher Scientific (Waltham, MA, USA). Solid-phase peptide syntheses were performed on an automated multichannel synthesizer Syro I (MultiSynTech, GmbH, Witten, Germany). Preparative RP-HPLC was performed on an LC-8A equipped with an SPD-M10 AV detector (both from Shimadzu, Kyoto, Japan) and a C18 Jupiter column (50 × 22 mm inner diameter; 10 μm; Phenomenex, Castel Maggiore, Italy). LC-MS analyses were performed on an LCQ DECA XP Ion Trap mass spectrometer equipped with an Opton Educational Services, Inc. source, operating at 4.2 kV needle voltage and 320°C, with a complete Surveyor HPLC system, comprising an MS pump, an autosampler, and a photo diode array (all from Thermo Fisher Scientific). The peptides reported in **Table 1** were synthesized by following standard fluorenylmethoxycarbonyl (Fmoc) strategies on a 50 μmol scale (33). To better mime the protein regions, the peptides investigated in this study were acetylated and amidated at the extremities. Rink-amide resin (substitution, 0.5 mmol/g) was used as the solid support. Activation of the amino acids was achieved with 2-(1*H*-benzotriazol-1-yl)-1,1,3,3-tetramethyluronium hexafuorophosphate (HBTU)/1-hydroxy-benzotriazole (HOBt)/di-isopropylethylamine (DIEA) (1:1:2), whereas Fmoc deprotection was performed with a 20% (v/v) piperidine solution in *N,N*-dimethylformamide (DMF). Peptides were removed from the resin by treatment with a TFA:tri-isopropylsilane (TIS):H_2O (90:5:5 v/v/v) mixture for 90 min at room temperature. The crude peptides were then precipitated in cold ether, dissolved in a water/acetonitrile (1:1 v/v) mixture, and lyophilized.

Products were purified by RP-HPLC, applying a linear gradient of 0.1% TFA CH_3CN in 0.1% TFA water from 5–65% over 12 min with a semipreparative 2.2 × 5 cm C18 column at a flow rate of 20 ml/min. Peptide purity identity was confirmed by LC-MS. Purified peptides were lyophilized and stored at −20°C until use.

Protein expression and purification

The coding sequence for NPM1-Cter-MutA, corresponding to residues 225–298 of the most common AML-associated mutant of NPM1 (26), was obtained through gene synthesis and cloned in a pGEX6P1 expression vector. NPM1-Cter-MutA was expressed from *Escherichia coli* BL21(DE3) cells and purified to homogeneity (30).

Far-UV circular dichroism spectroscopy

Samples were prepared by dilution of freshly prepared stock solutions (2 mM peptide on average), with peptide concentrations determined by UV absorbance with an ε_{275} value of 1390 $cm^{-1}\,M^{-1}$. Circular dichroism (CD) spectra were recorded on a J-815 spectropolarimeter (Jasco, Tokyo, Japan), registered at 25°C in the far-UV region from 190 to 260 nm. Other experimental settings were 20 nm/min scan speed, 2.0 nm band width, 0.2 nm resolution, 50 mdeg sensitivity, and 4 s response. Each spectrum was obtained with an average of 3 scans, subtracting contributions from corresponding blanks and converting the signal to mean residue ellipticity ($[\Theta]_{res}$) in units of degrees per square centimeter per decamole (deg cm^2 $dmol^{-1}$). The peptide concentration was 50 or 100 μM, and a 0.1 cm path-length quartz cuvette was used. For H2 $short^{265–272}$ and H2 $very\ short^{268–272}$, CD spectra were registered at 200 and 500 μM, respectively. For

TABLE 1. *Sequences of peptides based on H2 of the NPM1-CTD*

Name	Sequence	MW (amu)	pI
$H2^{264–277}$	^{264}VEAKFINYVKNCFR^{277}	1744.0	9.19
$K\text{-}H2^{263–277}$	^{263}KVEAKFINYVKNCFR^{277}	1901.2	9.63
$PK\text{-}H2^{262–277}$	^{262}PKVEAKFINYVKNCFR^{277}	1998.3	9.65
Nterm H2 $extended^{259–277}$	^{259}GSLPKVEAKFINYVKNCFR^{277}	2255.6	9.63
Nterm H2 ext. $mutated^{259–274}$	^{259}GSLPKVEAKFARLSIM^{274}	1789.1	9.99
Cterm H2 $extended^{264–280}$	^{264}VEAKFINYVKNCFRMTD^{280}	2120.4	8.15
N-, C-term H2 $extended^{259–280}$	^{259}GSLPKVEAKFINYVKNCFRMTD^{280}	2603.0	9.11
H2 $short^{265–272}$	^{265}EAKFINYV^{272}	1026.1	6.10
H2 $very\ short^{268–272}$	^{268}FINYV^{272}	696.7	5.52

MW (amu), molecular weight (atomic mass units).

NPM1-Cter-MutA, CD spectra were registered at 11 μM with a 0.2 cm path-length quartz cuvette. CD spectra were acquired in various buffers: 10 mM formiate (pH 3), 10 mM acetate (pH 5), 10 mM phosphate (pH 7), and 10 mM borate (pH 10). Temperature-dependent spectra were registered in the range of 298–368 K with a Peltier temperature controller.

Thioflavin T fluorescence assay

The thioflavin T (ThT) solution (6.48 μl; 38.5 mM in water) was added to 2.5 ml of the peptide stock solutions (the final concentrations of ThT and peptides were both 100 μM), whereas for NPM1-Cter-MutA, similar spectra were recorded at 16 and 20 μM, while the concentration of ThT was 20 μM at 25°C. ThT fluorescence was measured with a Varian Cary Eclipse spectrofluorimeter (Agilent Technologies, Stamford, CT, USA) and a quartz cuvette cell of 10 mm path-length, with magnetic stirring. Measurements were collected every 1–5 min for 60–240 min, and for NPM1-Cter-MutA until 13 days, with excitation and emission wavelengths of 440 and 450–600 nm, respectively.

Congo red absorbance assay

Interaction of Congo red (CR) with peptide aggregates was tested with a NanoDrop 2000, UV-Vis Spectrophotometer (Thermo Fisher Scientific) by recording the absorbance spectra from 400–800 nm with a 10 mm quartz cell. H2 peptides at 500 μM concentration and buffer as the control were incubated in 5 mM NaH_2PO_4 (pH 7.4) at 25°C, and an aliquot of 60 μL of each sample was mixed with 440 μl of a 5 mM NaH_2PO_4, 150 mM NaCl buffer (pH 7.4), containing 20 μM CR. Spectra were then recorded. The difference spectrum obtained by subtracting the spectrum of CR alone from that of CR^+ peptide indicated the spectrum of CR bound to the β-sheet structure.

Light-scattering measurements

$H2^{264–277}$ and Nterm H2 extended$^{259–277}$ (250 μM and 5 mM monomer concentrations, respectively) were kept in 10 mM borate buffer (pH 10) at 25°C, with constant stirring. The measurements were performed with a Zetasizer Nano S dynamic light-scattering (DLS) device (Malvern Instruments, Worcestershire, United Kingdom) with a 633 nm laser, in dual-scattering-angle mode, thermostated with a Peltier system, and a low-volume (45 μl), ultramicrocell. Size distributions by intensity and total light-scattering intensity were determined in automatic mode at regular time intervals over a period of 10 min for each measurement. Parameters were 13 acquisitions, each of 10-s duration.

AFM

$H2^{264–277}$ and Nterm H2 extended$^{259–277}$ peptides were incubated in 10 mM borate (pH 10) at 22°C. For AFM inspection, sample aliquots of 10 μL were extracted at different times during the aggregation reaction. Each aliquot was diluted 10-fold, and 10 μL of the diluted sample was deposited on a freshly cleaved mica substrate and dried in a mild vacuum. Tapping Mode AFM images were acquired in air with a Veeco Dimension 3100 Scanning Probe Microscope, equipped with a G scanning head (maximum scan size, 100 μm), and driven by a Nanoscope IIIa controller (Bruker, Billerica, MA, USA), and with a Multimode Scanning Probe Microscope equipped with an E scanning head (maximum scan size, 10 μm), driven by a Nanoscope V controller (Bruker). Single-beam uncoated silicon cantilevers (type OMCL-AC160TS; Olympus, Tokyo, Japan) were used. The drive frequency varied between 280 and 330 kHz, and the scan rate was between 0.2 and 0.8 Hz. Aggregate size was determined by the height in cross section of the topographic AFM images.

Cell cultures

Human SH-SY5Y neuroblastoma cells (American Type Culture Collection, Manassas, VA, USA) were cultured in DMEM/F-12 Ham's with 25 mM HEPES and $NaHCO_3$ (1:1) and supplemented with 10% fetal bovine serum, 1.0 mM glutamine, and antibiotics. Cell cultures were maintained in a 5.0% CO_2 humidified atmosphere at 37°C and grown until they reached 80% confluence for a maximum of 20 passages.

MTT reduction assay

SH-SY5Y cells were seeded in 96-well plates. Aggregates of $H2^{264–277}$, Nterm H2 extended$^{259–277}$, H2 short$^{265–272}$, and H2 very short$^{268–272}$ were incubated at concentrations of 100 μM (first 2 peptides) and 400 μM (last 2 peptides) in 10 mM borate buffer (pH 10) at 25°C, for 0, 1, and 15 h. The samples were centrifuged to collect the aggregates, which were resuspended in cell culture medium, all at a 100 μM peptide concentration, and then added to the SH-SY5Y cells for 24 h at 37°C. Cell viability was then assessed by the 3-(4,5-dimethylthiazol-2-yl)-2,5-diphenyltetrazolium bromide (MTT) reduction assay (34). In brief, the cell cultures were washed and incubated with 0.5 mg/ml MTT solution at 37°C for 4 h, and subsequently with cell lysis buffer (20% SDS, 50% DFM, pH 4.7) at 37°C for 3 h. Absorbances of blue formazan were determined at 590 nm, and cell viability was expressed as the percentage of MTT reduction in treated cells compared to that in untreated cells (taken as 100%).

Measurement of intracellular Ca^{2+}

Aggregates of $H2^{264–277}$, Nterm H2 extended$^{259–277}$, H2 short$^{265–272}$, and H2 very short$^{268–272}$ were incubated at concentrations of 100 μM (first 2 peptides) and 400 μM (last 2 peptides) in 10 mM borate buffer (pH 10) at 25°C for 0, 1, and 15 h. The samples were centrifuged to collect the aggregates, which were resuspended in cell culture medium, all at a 100 μM peptide concentration, and then added to SH-SY5Y cells seeded on glass coverslips for 60 min at 37°C. The cells were then loaded for 30 min at 37°C with 10 μM fluo3-AM (Life Technologies, Carlsbad, CA, USA) and 0.01% (w/v) pluronic acid F-127 in HBSS and subsequently fixed in 2% buffered paraformaldehyde for 10 min at room temperature. The resulting cell fluorescence was analyzed with a confocal scanning microscope (TCS SP5; Leica, Mannheim, Germany) equipped with an argon laser source for fluorescence measurements at 488 nm and a Plan Apo ×63 oil-immersion objective (Leica). A series of optical sections (1024 × 1024 pixels) 1.0 μm in thickness was taken through the cell depth for each examined sample. The confocal microscope was set at optimal acquisition conditions (*e.g.,* pinhole diameters, detector gain, and laser powers). The settings were maintained constant for each analysis. To quantify the signal intensity of the fluorescent probe, between 10 and 22 cells were analyzed with ImageJ software (National Institutes of Health, Bethesda, MD, USA), and the fluorescence intensities were expressed as arbitrary units.

Statistical analysis

Data are expressed as means ± SEM. Comparisons between the different groups were made by ANOVA followed by Bonferroni's post-comparison test. $P < 0.05$ was considered statistically significant.

RESULTS

On the basis of the sequence corresponding to the H2 region of the NPM1-CTD, 9 different peptides were synthesized and characterized. Most of the analyses were conducted on the fragment corresponding to the region 264–277 ($H2^{264–277}$), which constitutes H2 in the NMR structure of NPM1 (Fig. 1). Several longer and shorter variants of this prototypal peptide were also investigated. The sequences of all peptides are reported in Table 1. To properly mime the behavior of these regions in the real protein, all peptides were acetylated and amidated at the N and C termini, respectively. They were chemically synthesized with good yields by solid-phase peptide synthesis, by using Fmoc methodologies, and were purified by RP-HPLC. Their identity and purity (averaged purity, >97%) were assessed by LC-MS (data not shown).

The $H2^{264–277}$ peptide forms amyloidlike aggregates in physiologic conditions

A freshly dissolved solution of the $H2^{264–277}$ peptide in 10 mM phosphate buffer (pH 7), exhibited a characteristic β-sheet far-UV CD spectrum with a broad minimum at 218 nm (**Fig. 2*A***). The spectrum was virtually unchanged within 24 h, except for a slight decrease in the overall signal, probably resulting from the formation of large aggregates that escaped experimental detection. The large mean residue ellipticity (in the 215–220 nm range) indicated a β-sheet content similar to that of amyloid fibrils (35).

The conformational behavior of $H2^{264–277}$ was also evaluated as a function of pH. In 10 mM borate buffer at pH 10, the far-UV CD spectrum was identical with that registered at pH 7 (**Fig. 3*A***). In contrast, spectra collected at acidic pH, in 10 mM citrate buffer (pH 3) and 10 mM acetate buffer (pH 5), presented distinctive features: they were characterized by the presence of a minimum at ~207 nm and a shoulder at ~222 nm. These features are indicative of a mixture of conformational states (*i.e.*, random coil and α helix; Supplemental Fig. S3*A*).

The influence of pH on the conformational properties may be explained by considering the charge distribution in the peptide sequence. At acidic pH, the highly positive net charge of the peptide prevented the nearing of the molecules that leads to aggregation, whereas at neutral or basic pH, the positive charge was attenuated or cancelled, leading the peptide to self-assemble into β-sheet-containing aggregates. The influence of the temperature on $H2^{264–277}$ structure was also examined: β-structure-like CD spectra appeared stable upon the increase of temperature in the range 298–368 K, suggesting the presence of stable aggregates (Supplemental Fig. S4*A*). This is the typical behavior of an aggregated β structure that does not unfold at high temperature.

To gain insight into the propensity of $H2^{264–277}$ to aggregate, the time course of ThT fluorescence intensity in the presence of a freshly prepared solution of the peptide was monitored at 100 μM and pH 10 with stirring. ThT was chosen as the most common diagnostic dye of amyloidlike aggregates (36). The time dependence of the ThT fluorescence is generally suggestive of a nucleation-dependent growth mechanism that is typical for the kinetics of amyloid fibril formation. The aggregation of $H2^{264–277}$ showed this behavior but took place very quickly with a lag phase close to 0 (**Fig. 4*A***, **Table 2**). In addition, the ThT fluorescence was significantly high at time 0 [(~10 arbitrary units (au)], indicating that the peptide was aggregating, even at the start of the registered time course.

We also used the CR assay to assess whether $H2^{264–277}$ displays typical amyloid properties. Peptide concentration

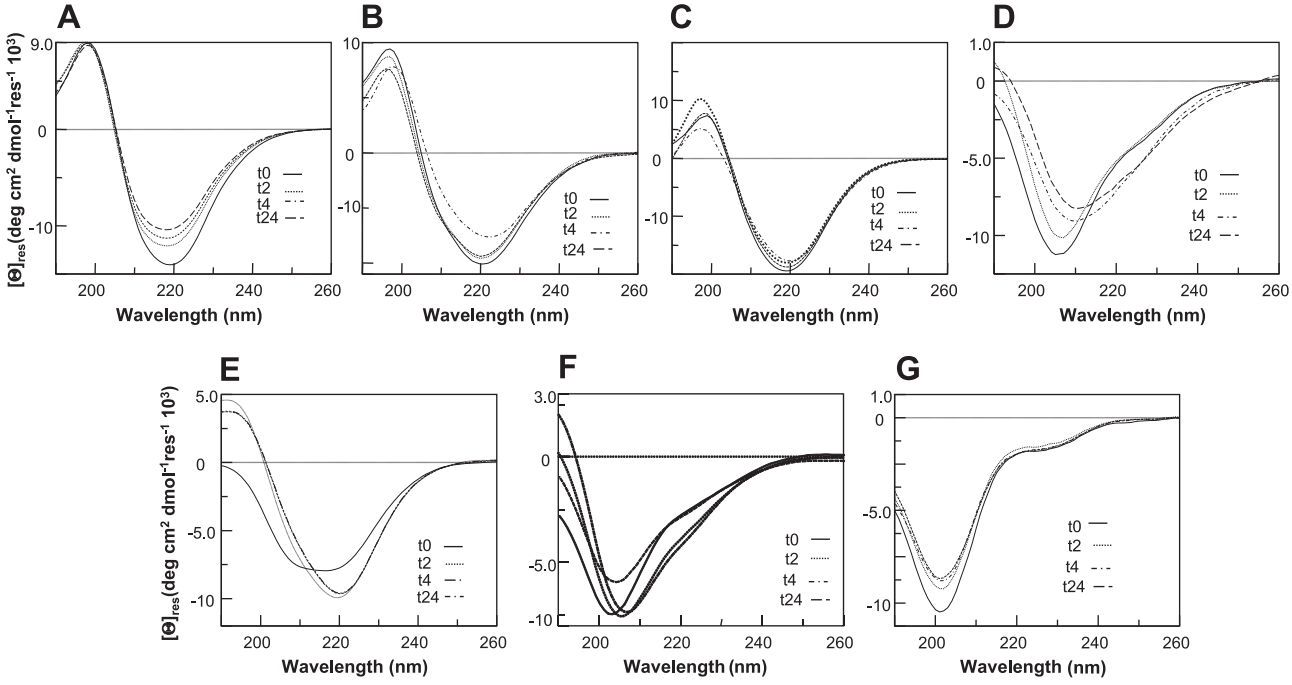

Figure 2. Overlay of CD spectra, recorded at 0, 2, 4, and 24 h from a fresh sample preparation, of (*A*) $H2^{264–277}$, (*B*) K-$H2^{263–277}$, (*C*) PK-$H2^{262–277}$, (*D*) Nterm H2 extended$^{259–277}$, (*E*) Cterm H2 extended$^{264–280}$, (*F*) N-, C-term H2 extended$^{259–280}$, and (*G*) Nterm H2 extended mutated$^{259–274}$, in 10 mM phosphate buffer (pH 7).

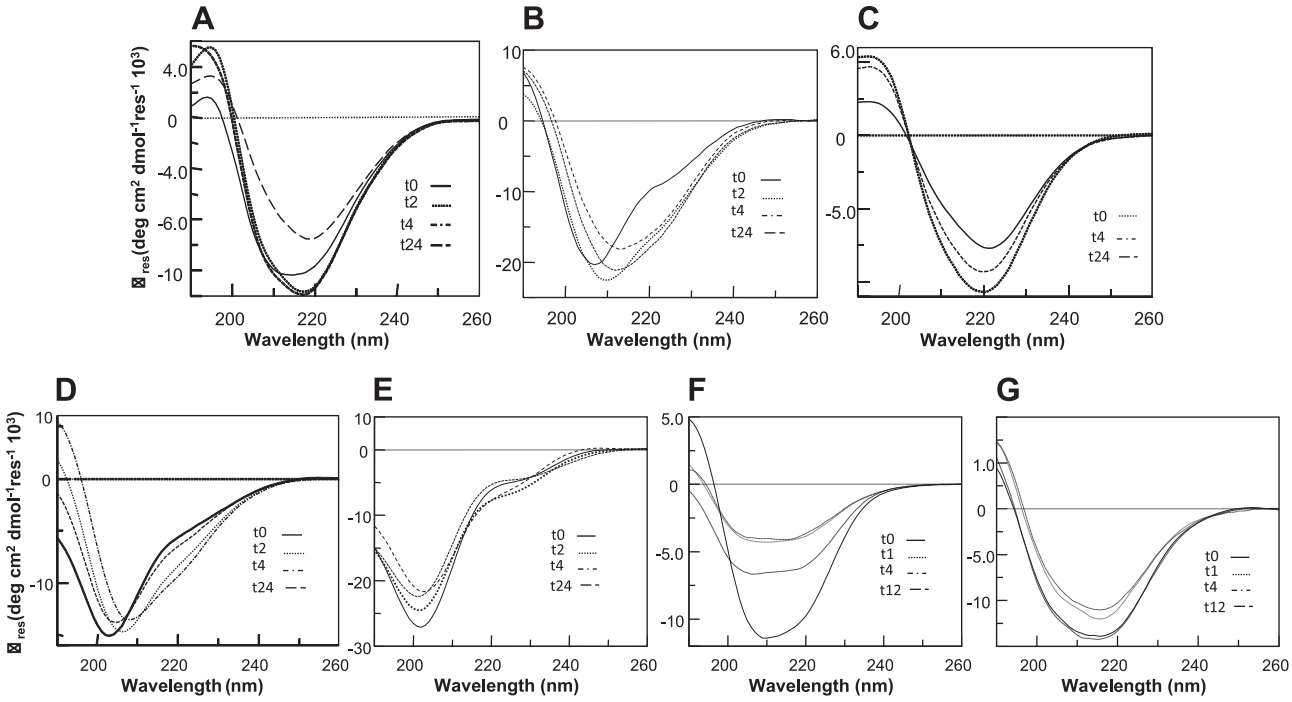

Figure 3. Overlay of CD spectra recorded at 0, 2, 4, and 24 h from a fresh sample preparation of (*A*) H2$^{264–277}$, (*B*) Nterm H2 extended$^{259–277}$, (*C*) Cterm H2 extended$^{264–280}$, (*D*) N-, C-term H2 extended$^{259–280}$, (*E*) Nterm H2 extended mutated$^{259–274}$, and at 0, 1, 4 and 12 h for (*F*) H2 short$^{265–272}$, and (*G*) H2 very short$^{268–272}$ in 10 mM borate buffer (pH 10).

was 500 μM, and pH was 7.4 in this case. The CR absorbance increased in the presence of the H2$^{264–277}$ peptide, and the wavelength of maximum absorption red shifted from 490 to 510 nm (Fig. 4*G*). The difference spectrum with a maximum at 550 nm indicated the presence of ordered aggregates with a β-sheet structure (Fig. 4*H*).

The extension of the H2 sequence limited its tendency to form amyloidlike aggregates

To investigate the role of the amino acid residues adjacent to H2 on the aggregation tendency of this CTD region, we designed and characterized longer variants by extending both its N- and C-terminal ends. In particular, at the N terminus we progressively added the residues of the region connecting H1 and H2 (*i.e.,* residues 259–263). At the C terminus, the 3 residues 278–280 connecting H2 to H3 were added (Table 1).

The CD spectra showed that the addition of Pro^{262} and Lys^{263} did not have a significant effect on the aggregation properties of H2 (Fig. 2*B, C*). In contrast, the addition of the fragment GSL$^{259–261}$ delayed the formation of the β-sheet structure (Fig. 2*D*). Indeed, in contrast to H2$^{264–277}$, the freshly dissolved Nterm H2 extended$^{259–277}$ peptide at pH 7 presented a CD spectrum characterized by a minimum at ~205 and a shoulder at 222 nm. These features are suggestive of a mixture of different secondary structure conformations. The evolution of the CD spectrum over time clearly indicated an enrichment of the β-structure content. Indeed a shift of the minimum from 205 to 213 nm occurred while the shoulder at ~222 nm disappeared. A similar behavior was shown at pH 10, although this conformational transition appeared to be more rapid (Fig. 3*B*).

The addition of 3 residues at the C terminus did not substantially influence the tendency of H2 to aggregate: in particular, the CD spectra of Cterm H2 extended$^{264–280}$ at neutral pH indicated a β transition in 2 h (Fig. 2*E*), and those at pH 10 indicated the presence of β-sheet aggregates, even at time 0 (Fig. 3*C*).

However, the concurrent extension at both the N and C termini clearly delayed the aggregation: even after 24 h, the CD spectrum of N-, C-term H2 extended$^{259–280}$ maintained features of a mixture of secondary structure conformations at both pH 7 and 10 (Figs. 2*F*, 3*D*).

In the ThT fluorescence assay, the time course of Nterm H2 extended$^{259–277}$ aggregation (Fig. 4*B*) at pH 10 presented a kinetic profile similar to that exhibited by H2$^{264–277}$ (Fig. 4*A*). However, the presence of the N-terminal extension delayed aggregation with respect to H2: the initial ThT fluorescence was lower than that observed for H2$^{264–277}$, a lag-phase of ~30 min was present, and the increase in ThT fluorescence was found to be slower, with a weak fluorescence, even after 160 min (Fig. 4*B*). The CR assay, performed after 1 d of incubation at pH 7.4, indicated spectral features for Nterm H2 extended$^{259–277}$ similar to those exhibited by H2$^{264–277}$ (Fig. 4*G*, *H*).

Similar to its effect on H2$^{264–277}$, an acidic pH condition did not cause substantial conformational transitions in any of the extended peptides (Supplemental Fig. S3*B–G*) and completely prevented peptide aggregation in the ThT assay (Fig. 4*C*).

Analysis of H2 aggregates by DLS and AFM

The aggregation of H2 peptides was further investigated by means of DLS (**Fig. 5*A***). A freshly prepared solution of H2$^{264–277}$ at pH 10 revealed the presence of aggregated

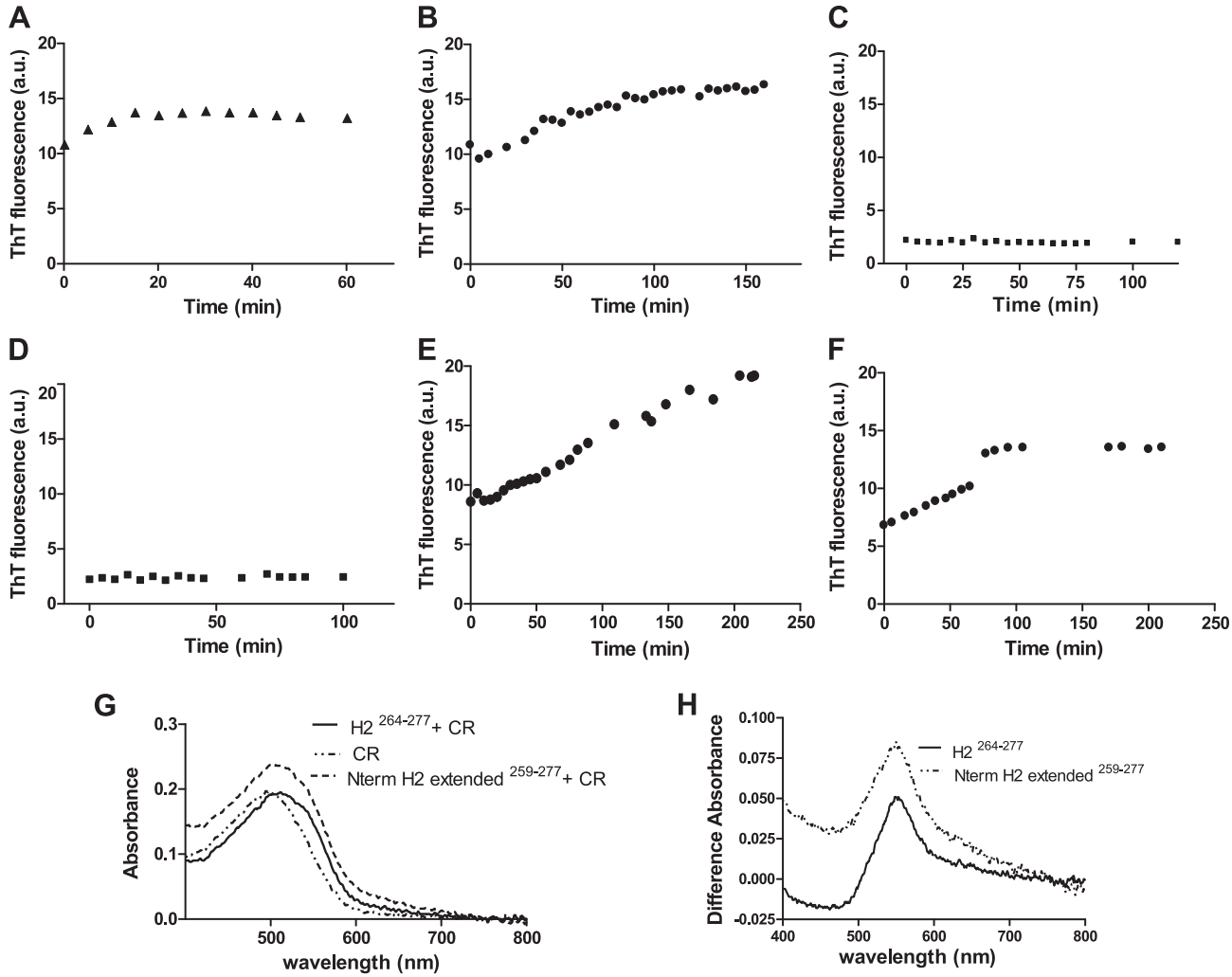

Figure 4. ThT and CR assays for the H2-based peptides. Time course of ThT fluorescence emission intensity at 480 nm for (*A*) $H2^{264–277}$ and (*B*) Nterm H2 extended$^{259–277}$ at pH 10; (*C*) Nterm H2 extended$^{259–277}$ at pH 5; and (*D*) Nterm H2 extended mutated$^{259–274}$, (*E*) H2 short$^{265–272}$, and (*F*) H2 very short$^{268–272}$ at pH 10. All assays at 100 μM peptide concentration. *G*) Absorbance spectra of $H2^{264–277}$+CR, CR, and Nterm H2 extended$^{259–277}$+CR. (H) Difference absorbance spectra obtained for $H2^{264–277}$ and Nterm H2 extended$^{259–277}$.

species. The analysis of the size distribution by the light-scattering intensity of the aggregated peptide showed 2 peaks centered at hydrodynamic diameters of ~50 nm (the most populated) and ~300 nm, respectively. After 4 h under stirring, the sample appeared cloudy. In another experiment, the same sample was immediately treated with hexafluoroisopropanol, which is a known disaggregating solvent of β-like structures (37), for 30 min at a concentration of 50% (v/v). After the removal of the organic solvent by evaporation, the DLS analysis of the solution did not show the presence of aggregates, as expected for a monomeric 13-mer peptide, with a hydrodynamic diameter that is probably less than the size limit of the instrument. These experiments confirmed that freshly prepared samples of $H2^{264–277}$ contain aggregates, as observed in the CD and ThT analyses.

TABLE 2. *Aggregation kinetics of peptides based on H2 of the NPM1-CTD at pH 10*

Name	Lag time (min)
$H2^{264–277}$	0
Nterm H2 extended$^{259–277}$	30
H2 short$^{265–272}$	22
H2 very short$^{268–272}$	0

Freshly dissolved Nterm H2 extended$^{259–277}$ at pH 10 displayed a different behavior, as the DLS analysis did not show the presence of any aggregate. Only after 30 h with stirring did the sample contain aggregates, with an intensity of scattering that showed 3 main peaks of hydrodynamic diameters centered at 30, 100, and 400 nm. (Supplemental Fig. S5*A*).

Tapping Mode atomic force microscopy (AFM; Bruker) was used to monitor the aggregation of $H2^{264–277}$ and Nterm H2 extended$^{259–277}$ peptides in 10 mM borate (pH 10). The $H2^{264–277}$ peptide was found to undergo rapid aggregation. Fibrillar aggregates were detected at the start of the experiment (not shown). At longer aggregation times, large clusters of fibrils were observed, with fibrils forming a closely intertwined mesh (Fig. 5*B*) The fibril height increased from 3.1 ± 0.2 nm at time (t) = 0 to 7.3 ± 0.4 nm at t = 30 min

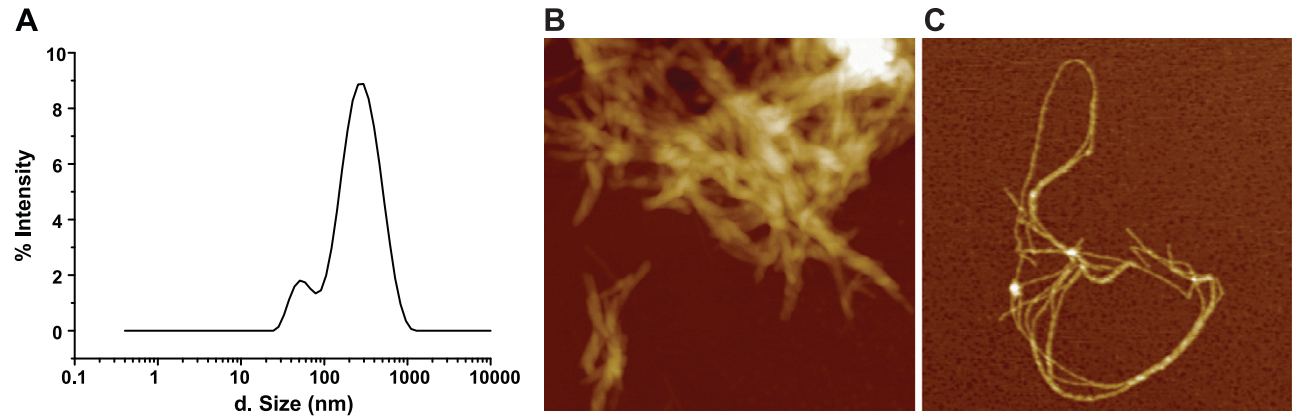

Figure 5. *A*) DLS intensity analysis of freshly prepared $H2^{264–277}$ oligomeric sample (monomeric concentration was 250 μM). *B*, *C*) Tapping Mode AFM images (height data; Bruker) of fibrillar aggregates formed by (*B*) $H2^{264–277}$ and (*C*) Nterm H2 extended$^{259–277}$ in 10 mM borate (pH 10), after (*B*) 1 and (*C*) 5 h. Scan size, 1.5 μm; *Z* range, (*B*) 110 and (*C*) 12 nm.

and 9.5 ± 0.5 nm after 1 h aggregation. The Nterm H2 extended$^{259–277}$ peptide displayed slower aggregation than $H2^{264–277}$. The fibrils were longer (Fig. 5*C*), and the fibril height did not change significantly with the aggregation time, being 3.7 ± 0.7 nm in the early stages of aggregation and 3.3 ± 0.4 nm after 10 h. For both peptides, the fibril morphologies and sizes are compatible with those commonly observed in amyloidlike aggregates.

The mutation of the H2 sequence suppressed its tendency to form amyloidlike aggregates

The role of the C-terminal region of H2 in the aggregation process was also investigated by the analysis of a peptide fragment generated from an NPM1 variant reported for AML with normal karyotype patients (38). This mutant is characterized by the deletion of the last 20 residues of the protein, beyond the H2 region, and by a completely different sequence for the 269–274 region, within H2 (Table 1). Because in this variant most of the residues of the pentapeptide, which likely represents the core of H2 aggregates, are changed, we evaluated the impact of these disease-associated modifications through the characterization of the fragment 259–274 of this form (Nterm H2 extended mutated$^{259–274}$). CD spectra collected over time for the peptide at both pH 7 and 10 indicated that it preferentially adopted a random coil structure in solution with a residual, albeit small, α-helical structure (Figs. 2*G*, 3*E*). No conversion of these conformers toward the β-sheet structure was detected in the explored time interval. Furthermore, the Nterm H2 extended mutated$^{259–274}$ peptide was not able to aggregate, because the ThT fluorescence signal did not increase over time, at pH 10 (Fig. 4*D*).

The pentapeptide 268–272, sequence FINYV, is the minimum H2 fragment that forms aggregates

The primary sequence of the NPM1-CTD was used as input to predict its tendency to form amyloidlike aggregates by using the PASTA server (*http://protein.bio.unipd.it/pasta2/*; University of Padua, Padua, Italy). This analysis unveiled that the H2 region has a strong intrinsic propensity to form amyloidlike aggregates and that the core of these aggregates corresponds to fragment 265–272, sequence EAKFINYV (**Fig. 6*A***). It is also worth noting that the sequence of the H2 region has a versatile conformational behavior, as it showed a tendency to adopt different states (α helix and β sheet) according to the NetCSSP (contact-dependent secondary structure propensity) server (39) (Fig. 6*B*).

According to these predictions, we sought to identify the shortest H2 fragment that forms amyloidlike assemblies. Therefore, experiments similar to those performed with $H2^{264–277}$ at pH 10 were performed on the fragment 265–272 EAKFINYV (H2 short$^{265–272}$). The CD spectra of this peptide at pH 10 appeared quite different over time; indeed, the freshly prepared sample provided a helicallike CD-spectrum that after 12 h presented only a broad minimum at 210 nm (Fig. 3*F*). This behavior is supported by the observation that the fragment displays a good propensity for adopting either an α-helical or a β-sheet conformation (Fig. 6*B*). However, this peptide had a strong tendency to aggregate and precipitate, as shown by the relatively fast CD signal decrease over time (Fig. 3*F*). The formation of amyloidlike aggregates by this peptide was confirmed by the ThT assay (Fig. 4*E*).

The sequence of H2 short$^{265–272}$ was characterized by the presence of charged amino acid residues at its N terminus and a hydrophobic stretch at the C terminus. We therefore evaluated the ability of the hydrophobic pentapeptide FINYV to aggregate independently (H2 very short$^{268–272}$). The analysis of the CD spectrum at pH 10 clearly indicated that this fragment had a strong tendency to form β-sheet aggregates (Fig. 3*G*). Notably, the structural features of this peptide did not show any significant variation in the temperature range 298–368 K (Supplemental Fig. S4*B*). Moreover, H2 very short$^{268–272}$ showed a great propensity to form amyloid aggregates, as shown by the ThT assay, with faster kinetics than those of H2 short$^{265–272}$ (Fig. 4*F*, Table 2).

H2-derived peptides induce cytotoxicity and intracellular Ca^{2+} influx in SH-SY5Y cells

The H2-derived peptides were also evaluated for their ability to impair cell viability. We first analyzed the effects

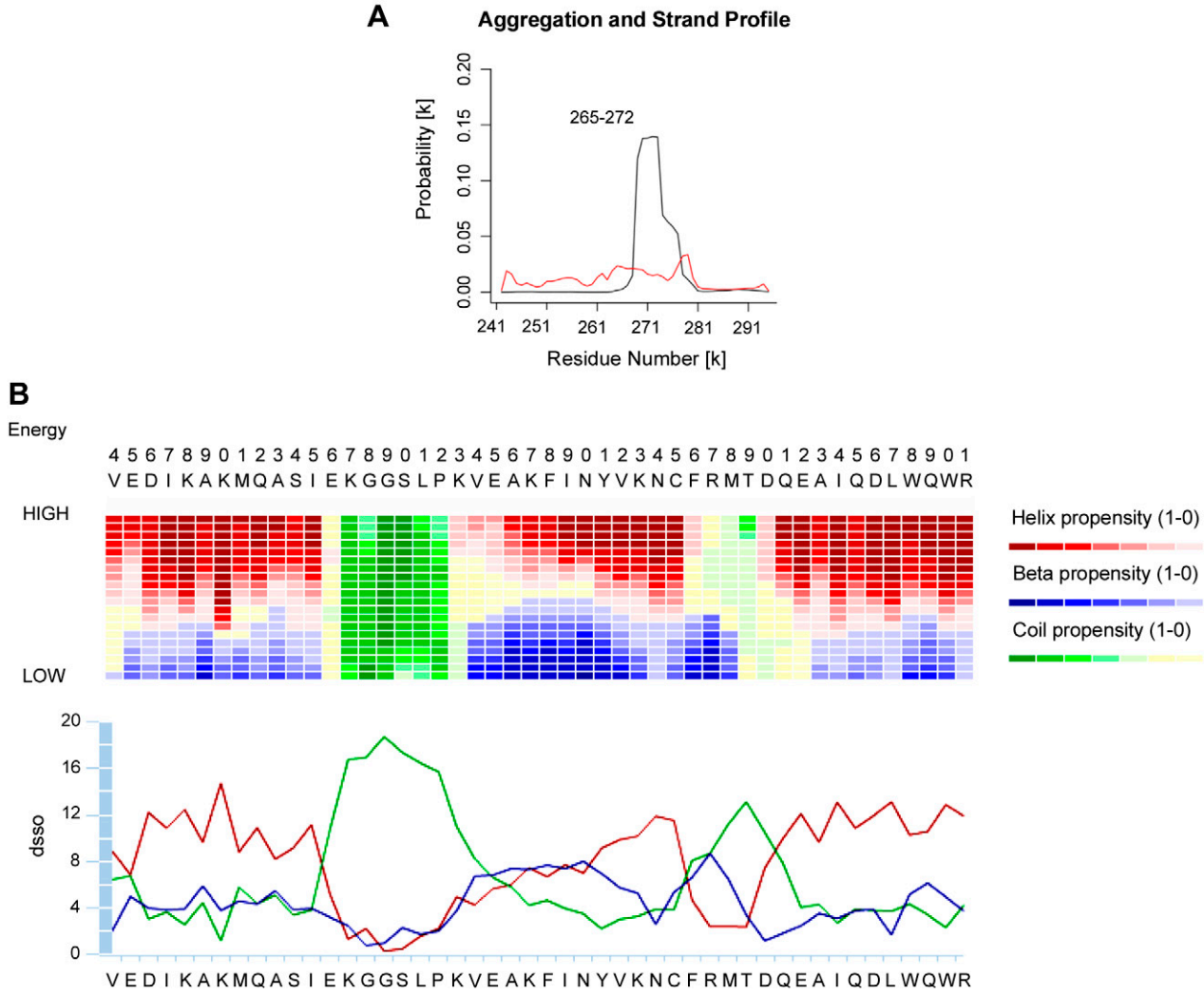

Figure 6. Prediction of (*A*) amyloidlike aggregation determined using PASTA. (*B*) Chameleon profile using NetCSSP of NPM1-CTD.

of the aggregates formed from the H2 peptides on the mitochondrial status by measuring the MTT reduction assay in human SH-SY5Y neuroblastoma cells. Samples from $H2^{264–277}$, Nterm H2 extended$^{259–277}$, H2 short$^{265–272}$, and H2 very short$^{268–272}$ were incubated at a monomer equivalent concentration of 100 μM at 3 different times (0, 1, and 15 h) and then added to the cells. Aggregates of $H2^{264–277}$ showed the highest toxicity at 0 and 1 h, becoming almost ineffective after 15 h of incubation (**Fig. 7**), whereas aggregates of Nterm H2 extended$^{259–277}$ showed the main toxicity after 15 h of incubation. Aggregated H2 short$^{265–272}$ and H2 very short$^{268–272}$ were found to be toxic both at the short and long times, although the toxicity was slightly lower at 15 h, relative to the earlier times. The decrease in toxicity with aggregation time for $H2^{264–277}$, H2 short$^{265–272}$, and H2 very short$^{268–272}$ probably arises from the conversion of the early aggregates into larger aggregates or mature fibrils, which are known to be less toxic than the first oligomeric species (40–43). By contrast, the increase in toxicity with aggregation time observed for the Nterm H2 extended$^{259–277}$ peptide is likely to result from the slower aggregation process of this peptide. The comparison between the toxicities found at 0 and 1 h indicates that the extended and shortened versions of the H2 peptides are less and more toxic than $H2^{264–277}$, respectively.

It is widely accepted that disruption of intracellular Ca^{2+} homeostasis is one of the earliest biochemical consequences of the interaction of prefibrillar aggregates with cell membranes (44, 45). We therefore investigated the effects of aggregated H2 peptides on the Ca^{2+} content of SH-SY5Y cells. Aggregates of $H2^{264–277}$ were found to cause a large influx of extracellular Ca^{2+} ions into the cytosol at the 0 and 1 h aggregation times, becoming less toxic after 15 h (**Fig. 8**). By contrast, aggregates of Nterm H2 extended$^{259–277}$ were weakly toxic at 0 and 1 h and caused the main Ca^{2+} influx after 15 h of aggregation time. Aggregates of H2 short$^{265–272}$ and H2 very short$^{268–272}$ were found to lead to a strong increase in intracellular Ca^{2+}, at both the short and long times, although the effect was less marked at 15 h. Overall, the Ca^{2+} influx caused by the aggregated peptides showed a trend similar to that observed for the MTT reduction assay (Fig. 7). Hence, the comparison between the effects found at 0 and 1 h indicate that the extended and shortened versions of the H2 peptides were less and more toxic than $H2^{264–277}$, respectively.

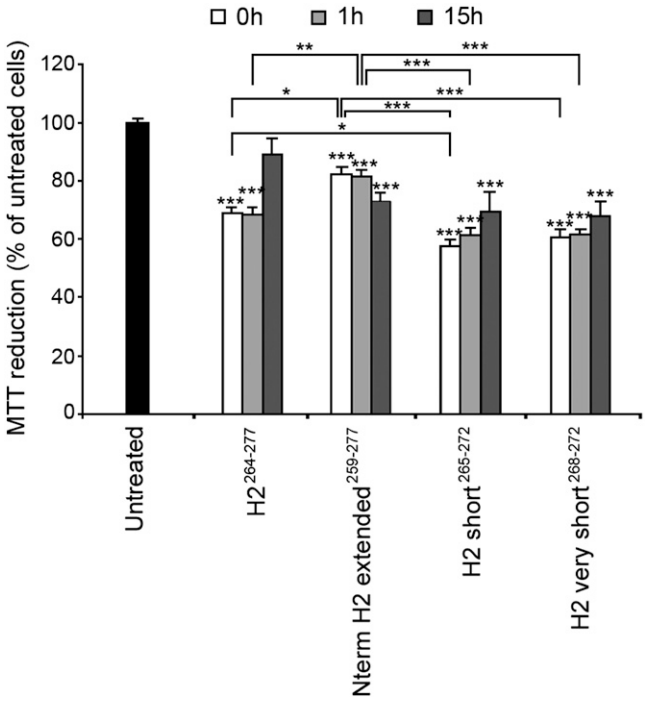

Figure 7. Cytotoxicity of aggregates formed by H2 peptides. Aggregates of $H2^{264–277}$, Nterm H2 extended$^{259–277}$, H2 short$^{265–272}$, and H2 very short$^{268–272}$ (100 μM monomer concentration) were formed at 3 different times (0, 1, and 15 h) and added to human SH-SY5Y neuroblastoma cells. Cell viability was expressed as the percentage of MTT reduction in the treated cells, compared with that in the untreated cells (taken to be 100%). The values shown are means ± SEM of results in 3 independent experiments performed in triplicate. $*P \leq 0.05$, $**P \leq 0.01$, $***P \leq 0.001$ *vs.* untreated cells, unless otherwise indicated.

NPM1-Cter-MutA tends to slowly aggregate

We purified the CTD of the most common AML-associated mutant of NPM1 (26), corresponding to residues 225–298 of the mutated NPM1 protein (NPM1-Cter-MutA). ThT fluorescence spectra were registered at different time points in the presence of NPM1-Cter-MutA at 16 μM, with stirring (pH 10). This analysis revealed a progressive increase in fluorescence intensity within 13 d, suggesting a rather slow formation of amyloidlike species (**Fig. 9*A***). This trend was confirmed by similar experiments performed at the slightly higher concentration of 20 μM (data not shown).

Furthermore, CD analysis over 8 d with constant stirring (pH 10) revealed that NPM1-Cter-MutA tended to aggregate, suggested by the progressive decrease in CD signal intensity over time (Fig. 9*B*).

A deeper analysis of the overlay of CD spectra registered at different times did not show significant variations of the overall shape of the spectrum (*i.e.,* location of the minima). This finding suggests that the protein region involved in the aggregation process is rather limited.

DISCUSSION

The CTD of NPM1 is an essential element for the activities of this multifunction protein. It is crucial for shuttling and for its interactions with DNA (6, 23, 31), and its functionality relies on the specific fold that it adopts: a 3-helix bundle. Investigations have indicated that the 3 helical regions of the domain are endowed with a high intrinsic propensity for this structural element (9, 12). Nevertheless, the results in this study show that, in physiologic conditions, the fragment corresponding to the α-H2 forms amyloidlike cytotoxic aggregates. *A posteriori* bioinformatics analyses confirm the chameleonic nature of this region.

The inspection of the sequence highlights the presence of several charged residues that usually hamper the formation of amyloidlike aggregates. The longest fragment that maintains a significant tendency to form β-structured aggregates (Nterm H2 extended$^{259–277}$) presents a basic isoelectric point (pI), due to the presence of 3 lysine and 1 arginine residues and a single glutamic acid residue. This observation explains the increased tendency of the peptide to form β-structured aggregates when the pH is shifted from 3 or 5 (no aggregation), to 7 (very slow aggregation), to 10 (slow aggregation). Indeed, the reduction of the overall positive charge of the peptide from pH 7 to 10, which is due to the full or partial deprotonation of the positively charged residues, favors aggregation, whereas the further accumulation of positive charges from pH 7 to acidic pH values inhibit self-assembly.

Nevertheless, the ability of the $H2^{264–277}$, K-$H2^{263–277}$, and PK-$H2^{262–277}$ peptides to readily aggregate into a β structure at pH 7 indicates that the formation of this assembly is compatible with the presence of several charged residues. In a putative aggregate formed by the packing of 2 adjacent β sheets, it is unlikely that these charged residues are inserted in the dry interface of the interacting β sheets. By considering that, in a β strand, the positioning of the side chains alternates with respect to the backbone, the analysis of the specific sequence of this fragment shows an intriguing finding: that all charged residues are positioned on the same face of the sheet. If we assume that this is an external face of a 2-sheet aggregate, the dry core of this β structure likely involves some or all of the following residues: Val^{264}, Ala^{266}, Phe^{268}, Asn^{270}, Val^{272}, Asn^{274}, and Phe^{276}. It is important to note that these types of residues are frequently found at the dry interfaces of the steric zipper assemblies characterized by Eisenberg *et al.* (46, 47).

Present data show that the extension of the N- and C-terminal ends of the H2 peptide, to include the connecting regions with H1 and H3, delays its aggregation. The most evident effect is produced by the inclusion of the GSL (259–261) trait at the N terminus. The apolar side chain of Leu^{261}, which also forms hydrophobic interactions with the Tyr^{271} side chain in the folded 3-helix bundle (Protein Data Base code 2VLD; maintained by the Research Collaboratory for Structural Bioinformatics; http://www.rcsb.org/pdb/static.do?p=general_information/about_pdb/index.html), establishes interactions with the numerous apolar side chains of the peptide, disfavoring the process of formation of the β-structured assembly. In addition, both Gly^{259} [intrinsically low propensity to adopt β structure (48)] and Ser^{260} for its polarity (49) are also unconstructive for β-sheet aggregation. These considerations add to the presence of Pro^{262} and Lys^{263}, which are a β-breaker (50) and a charged residue, respectively, and further increase the net charge.

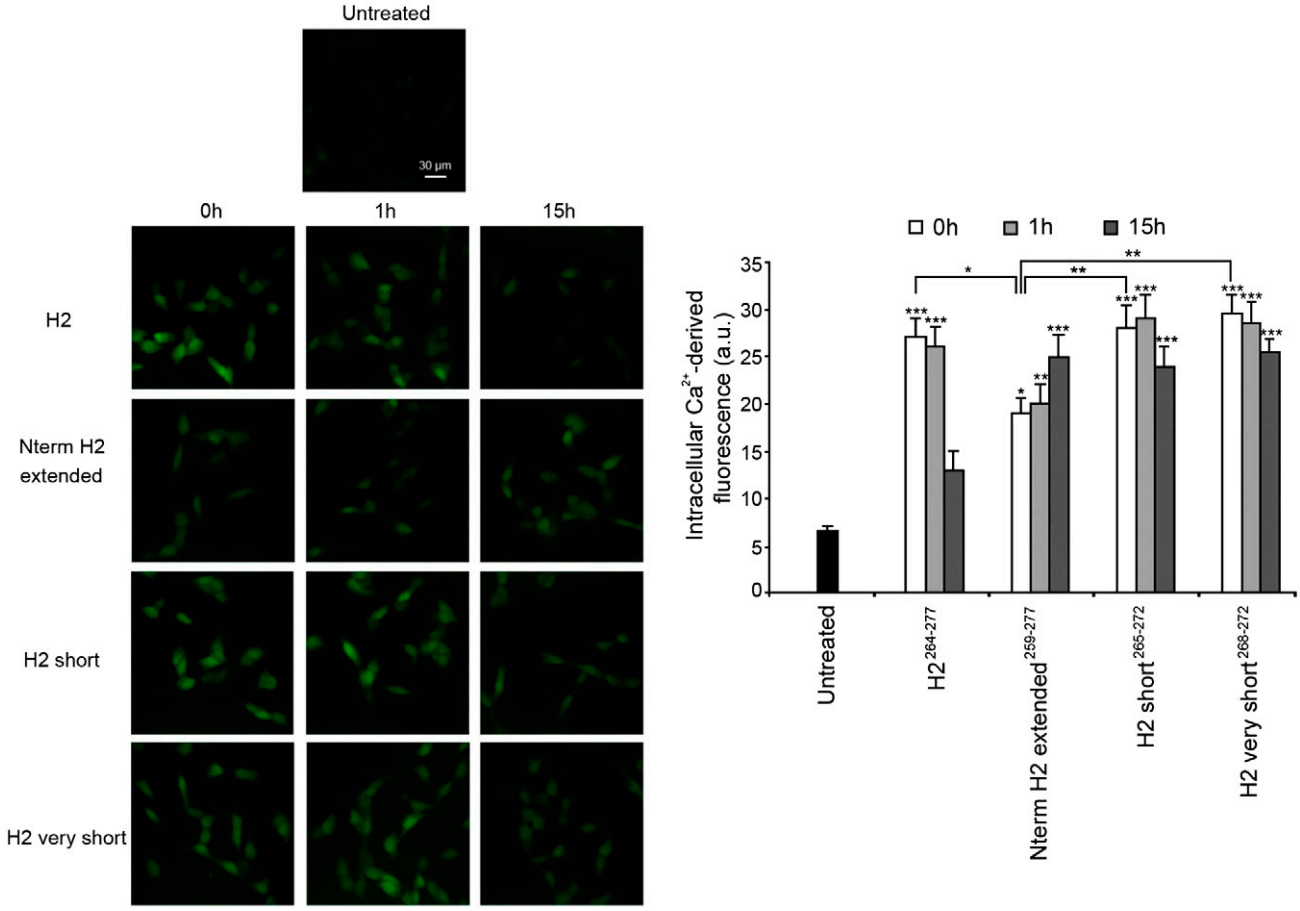

Figure 8. Representative confocal scanning microscope images showing intracellular Ca^{2+} levels in SH-SY5Y cells. Aggregates of $H2^{264–277}$, Nterm H2 extended$^{259–277}$, H2 short$^{265–272}$, and H2 very short$^{268–272}$ (100 μM monomer concentration) were formed at 3 different times (0, 1, and 15 h) and added to the cells for 60 min. The green fluorescence arises from the intracellular Fluo3 probe bound to Ca^{2+}. The corresponding semiquantitative values of the green fluorescence signals are shown below the images. The values shown are means ± SEM of results in 3 independent experiments performed in triplicate. $*P \leq 0.05$, $**P \leq 0.01$, $***P \leq 0.001$ *vs.* untreated cells, unless otherwise indicated.

These observations suggest that the local context has an impact on the aggregation tendency of H2 and have implications for the aggregation propensity of the entire CTD. It has been reported that the thermally and chemically denatured states of NPM1-CTD retain significant residual structure mainly at the interface between H2 and H3 (10, 11) and that this compact denatured state is stable over time (9–11). Our experiments show that the wild-type (wt) CTD of NPM1 does not possess any tendency to aggregate (data not

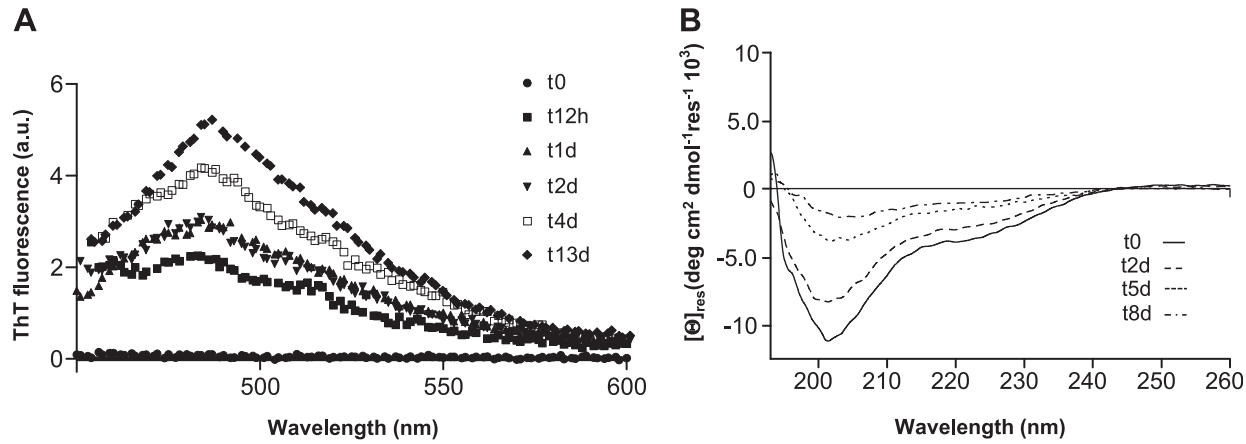

Figure 9. Tht and CD assay analysis of NPM1-Cter-MutA. *A*) ThT fluorescence emission spectra in the presence of NPM1-CterMutA (at 16 μM) registered at 0 and 12 h and 1, 2, 4, and 13 d. *B*) CD spectra recorded at 0, 2, 5, and 8 d at a concentration of NPM1-CterMutA of 11 μM, with stirring.

shown). Collectively, these considerations indicate that the residual interactions involving H2 and stabilizing its α-helical structure in the NPM1-CTD denatured state prevent amyloidlike aggregation. It has been shown that the stabilization of the α-helical structure can cause an acceleration of the aggregation process, depending on the initial stability and location of the α-helices (51). In particular, the effect can vary if the stabilized helices are *1*) in nonamyloidogenic stretches of initially unstructured peptides (accelerating effect), *2*) in amyloidogenic stretches of initially unstructured peptides (no effect), or *3*) in amyloidogenic stretches of initially stable helices (decelerating effect). Given the significant stability of H2 in the denatured wt CTD and the observation that H2 is an amyloidogenic stretch, the tendency of the wt CTD to unfold through compact states retaining residual α-helical structure may be a protective mechanism that prevents unwanted and potentially harmful aggregation. Therefore, not only folded states, but also compact unfolded ones, are effective for escaping misfolding and aggregation. It is also possible that the chaperone activity of the N-terminal domain of NPM1 (16, 30), which has stabilizing effects on the CTD (9), plays, among others, a role in preventing the misfolding of NPM1-CTD in the full-length protein.

Present findings may have implications for understanding AML-NPM1 mutants. Indeed, these mutants present specific features (20, 52, 53): *1*) mutations cause the aberrant accumulation of NPM1 variants in the cytoplasm ($NPM1c^+$); *2*) mutated proteins acquire some new properties (gain of function), along with expected loss of protein functionality (loss of function); and *3*) mutations are common in adult AML (~30% of cases), but occur less frequently in children (6.5–8.4%) (52). In this scenario, the absence of strong intramolecular interactions in the unfolded mutated CTDs and the accumulation of the mutants into the cytoplasm may favor aggregation through the exposure of the amyloidogenic H2 region. The slow aggregation shown by NPM1-Cter-MutA domain confirms our hypothesis. The formation of cytoplasmic aggregates may, in turn, be involved in the observed gain of function and in the pathogenesis of the disease. Indeed, the observation that H2 amyloidlike assemblies are cytotoxic suggests that they are active biologic entities and that they may be involved in the gain of function observed in NPM1 mutants. It is worth mentioning that our data also show that the H2 region of a rather rare exon 11 mutation, which is associated with AML and characterized by a prevalent nucleolar localization (37), has no tendency to form amyloidlike aggregates, suggesting that a different pathogenic mechanism is at work in this case. Nevertheless, it can be speculated that the lower accumulation of this mutant into the cytoplasm (37) is somewhat related to its inability to aggregate.

In conclusion, although a link between prionlike aggregation and cancer has been proposed and currently has been investigated only in p53 mutants (54), we believe that the possible link between aggregation of NPM1 and AML should be seriously considered in studies aimed at unveiling the molecular mechanisms of this severe, widespread disease. FJ

This work was funded in part by Regione Campania Rete integrated network for the biotechnology applied to molecules with pharmacological activity; FarmaBioNet, the intervention biotechnology for the development of new drugs (Bando per la Realizzazione della Rete delle Biotecnologie Campane, Obiettivo Operativo 2.1 POR Campania).

REFERENCES

1. Kang, Y. J., Olson, M. O., Jones, C., and Busch, H. (1975) Nucleolar phosphoproteins of normal rat liver and Novikoff hepatoma ascites cells. *Cancer Res.* **35**, 1470–1475
2. Okuwaki, M., Matsumoto, K., Tsujimoto, M., and Nagata, K. (2001) Function of nucleophosmin/B23, a nucleolar acidic protein, as a histone chaperone. *FEBS Lett.* **506**, 272–276
3. Namboodiri, V. M., Akey, I. V., Schmidt-Zachmann, M. S., Head, J. F., and Akey, C. W. (2004) The structure and function of Xenopus NO38-core, a histone chaperone in the nucleolus. *Structure* **12**, 2149–2160
4. Lee, H. H., Kim, H. S., Kang, J. Y., Lee, B. I., Ha, J. Y., Yoon, H. J., Lim, S. O., Jung, G., and Suh, S. W. (2007) Crystal structure of human nucleophosmin-core reveals plasticity of the pentamer-pentamer interface. *Proteins* **69**, 672–678
5. Mitrea, D. M., Grace, C. R., Buljan, M., Yun, M. K., Pytel, N. J., Satumba, J., Nourse, A., Park, C. G., Madan Babu, M., White, S. W., and Kriwacki, R. W. (2014) Structural polymorphism in the N-terminal oligomerization domain of NPM1. *Proc. Natl. Acad. Sci. USA* **111**, 4466–4471
6. Arcovito, A., Chiarella, S., Della Longa, S., Di Matteo, A., Lo Sterzo, C., Scaglione, G. L., and Federici, L. (2014) Synergic role of nucleophosmin three-helix bundle and a flanking unstructured tail in the interaction with G-quadruplex DNA. *J. Biol. Chem.* **289**, 21230–21241
7. Scognamiglio, P. L., Di Natale, C., Leone, M., Poletto, M., Vitagliano, L., Tell, G., and Marasco, D. (2014) G-quadruplex DNA recognition by nucleophosmin: new insights from protein dissection. *Biochim. Biophys. Acta* **1840**, 2050–2059
8. Grummitt, C. G., Townsley, F. M., Johnson, C. M., Warren, A. J., and Bycroft, M. (2008) Structural consequences of nucleophosmin mutations in acute myeloid leukemia. *J. Biol. Chem.* **283**, 23326–23332
9. Marasco, D., Ruggiero, A., Vascotto, C., Poletto, M., Scognamiglio, P. L., Tell, G., and Vitagliano, L. (2013) Role of mutual interactions in the chemical and thermal stability of nucleophosmin NPM1 domains. *Biochem. Biophys. Res. Commun.* **430**, 523–528
10. Scaloni, F., Gianni, S., Federici, L., Falini, B., and Brunori, M. (2009) Folding mechanism of the C-terminal domain of nucleophosmin: residual structure in the denatured state and its pathophysiological significance. *FASEB J.* **23**, 2360–2365
11. Scaloni, F., Federici, L., Brunori, M., and Gianni, S. (2010) Deciphering the folding transition state structure and denatured state properties of nucleophosmin C-terminal domain. *Proc. Natl. Acad. Sci. USA* **107**, 5447–5452
12. Chiarella, S., Federici, L., Di Matteo, A., Brunori, M., and Gianni, S. (2013) The folding pathway of a functionally competent C-terminal domain of nucleophosmin: protein stability and denatured state residual structure. *Biochem. Biophys. Res. Commun.* **435**, 64–68
13. Marasco, D., and Scognamiglio, P. L. (2015) Identification of inhibitors of biological interactions involving intrinsically disordered proteins. *Int. J. Mol. Sci.* **16**, 7394–7412
14. Okuwaki, M. (2008) The structure and functions of NPM1/nucleophsmin/B23, a multifunctional nucleolar acidic protein. *J. Biochem.* **143**, 441–448
15. Herrera, J. E., Savkur, R., and Olson, M. O. (1995) The ribonuclease activity of nucleolar protein B23. *Nucleic Acids Res.* **23**, 3974–3979
16. Murano, K., Okuwaki, M., Hisaoka, M., and Nagata, K. (2008) Transcription regulation of the rRNA gene by a multifunctional nucleolar protein, B23/nucleophosmin, through its histone chaperone activity. *Mol. Cell. Biol.* **28**, 3114–3126
17. Okuwaki, M., Iwamatsu, A., Tsujimoto, M., and Nagata, K. (2001) Identification of nucleophosmin/B23, an acidic nucleolar protein, as a stimulatory factor for in vitro replication of adenovirus DNA complexed with viral basic core proteins. *J. Mol. Biol.* **311**, 41–55
18. Lindström, M. S. (2011) NPM1/B23: a multifunctional mhaperone in mibosome biogenesis and chromatin remodeling. *Biochem. Res. Int.* **2011**, 195209

19. Colombo, E., Alcalay, M., and Pelicci, P. G. (2011) Nucleophosmin and its complex network: a possible therapeutic target in hematological diseases. *Oncogene* **30**, 2595–2609
20. Grisendi, S., Mecucci, C., Falini, B., and Pandolfi, P. P. (2006) Nucleophosmin and cancer. *Nat. Rev. Cancer* **6**, 493–505
21. Maggi, L. B., Jr., Kuchenruether, M., Dadey, D. Y., Schwope, R. M., Grisendi, S., Townsend, R. R., Pandolfi, P. P., and Weber, J. D. (2008) Nucleophosmin serves as a rate-limiting nuclear export chaperone for the mammalian ribosome. *Mol. Cell. Biol.* **28**, 7050–7065
22. Yun, J. P., Miao, J., Chen, G. G., Tian, Q. H., Zhang, C. Q., Xiang, J., Fu, J., and Lai, P. B. (2007) Increased expression of nucleophosmin/B23 in hepatocellular carcinoma and correlation with clinicopathological parameters. *Br. J. Cancer* **96**, 477–484
23. Poletto, M., Lirussi, L., Wilson III, D. M., and Tell, G. (2014) Nucleophosmin modulates stability, activity, and nucleolar accumulation of base excision repair proteins. *Mol. Biol. Cell* **25**, 1641–1652
24. Balusu, R., Fiskus, W., Rao, R., Chong, D. G., Nalluri, S., Mudunuru, U., Ma, H., Chen, L., Venkannagari, S., Ha, K., Abhyankar, S., Williams, C., McGuirk, J., Khoury, H. J., Ustun, C., and Bhalla, K. N. (2011) Targeting levels or oligomerization of nucleophosmin 1 induces differentiation and loss of survival of human AML cells with mutant NPM1. *Blood* **118**, 3096–3106
25. Bolli, N., De Marco, M. F., Martelli, M. P., Bigerna, B., Pucciarini, A., Rossi, R., Mannucci, R., Manes, N., Pettirossi, V., Pileri, S. A., Nicoletti, I., and Falini, B. (2009) A dose-dependent tug of war involving the NPM1 leukaemic mutant, nucleophosmin, and ARF. *Leukemia* **23**, 501–509
26. Falini, B., Martelli, M. P., Bolli, N., Bonasso, R., Ghia, E., Pallotta, M. T., Diverio, D., Nicoletti, I., Pacini, R., Tabarrini, A., Galletti, B. V., Mannucci, R., Roti, G., Rosati, R., Specchia, G., Liso, A., Tiacci, E., Alcalay, M., Luzi, L., Volorio, S., Bernard, L., Guarini, A., Amadori, S., Mandelli, F., Pane, F., Lo-Coco, F., Saglio, G., Pelicci, P. G., Martelli, M. F., and Mecucci, C. (2006) Immunohistochemistry predicts nucleophosmin (NPM) mutations in acute myeloid leukemia. *Blood* **108**, 1999–2005
27. Falini, B., Mecucci, C., Tiacci, E., Alcalay, M., Rosati, R., Pasqualucci, L., La Starza, R., Diverio, D., Colombo, E., Santucci, A., Bigerna, B., Pacini, R., Pucciarini, A., Liso, A., Vignetti, M., Fazi, P., Meani, N., Pettirossi, V., Saglio, G., Mandelli, F., Lo-Coco, F., Pelicci, P. G., and Martelli, M. F.; GIMEMA Acute Leukemia Working Party. (2005) Cytoplasmic nucleophosmin in acute myelogenous leukemia with a normal karyotype. *N. Engl. J. Med.* **352**, 254–266
28. Falini, B., Nicoletti, I., Bolli, N., Martelli, M. P., Liso, A., Gorello, P., Mandelli, F., Mecucci, C., and Martelli, M. F. (2007) Translocations and mutations involving the nucleophosmin (NPM1) gene in lymphomas and leukemias. *Haematologica* **92**, 519–532
29. Falini, B., Nicoletti, I., Martelli, M. F., and Mecucci, C. (2007) Acute myeloid leukemia carrying cytoplasmic/mutated nucleophosmin (NPMc+ AML): biologic and clinical features. *Blood* **109**, 874–885
30. Okuwaki, M., Sumi, A., Hisaoka, M., Saotome-Nakamura, A., Akashi, S., Nishimura, Y., and Nagata, K. (2012) Function of homo- and hetero-oligomers of human nucleoplasmin/nucleophosmin family proteins NPM1, NPM2 and NPM3 during sperm chromatin remodeling. *Nucleic Acids Res.* **40**, 4861–4878
31. Chiarella, S., De Cola, A., Scaglione, G. L., Carletti, E., Graziano, V., Barcaroli, D., Lo Sterzo, C., Di Matteo, A., Di Ilio, C., Falini, B., Arcovito, A., De Laurenzi, V., and Federici, L. (2013) Nucleophosmin mutations alter its nucleolar localization by impairing G-quadruplex binding at ribosomal DNA. *Nucleic Acids Res.* **41**, 3228–3239
32. Leong, S. M., Tan, B. X., Bte Ahmad, B., Yan, T., Chee, L. Y., Ang, S. T., Tay, K. G., Koh, L. P., Yeoh, A. E., Koay, E. S., Mok, Y. K., and Lim, T. M. (2010) Mutant nucleophosmin deregulates cell death and myeloid differentiation through excessive caspase-6 and -8 inhibition. *Blood* **116**, 3286–3296
33. Fields, G. B., and Noble, R. L. (1990) Solid phase peptide synthesis utilizing 9-fluorenylmethoxycarbonyl amino acids. *Int. J. Pept. Protein Res.* **35**, 161–214
34. Mosmann, T. (1983) Rapid colorimetric assay for cellular growth and survival: application to proliferation and cytotoxicity assays. *J. Immunol. Methods* **65**, 55–63
35. Martins, I. C., Kuperstein, I., Wilkinson, H., Maes, E., Vanbrabant, M., Jonckheere, W., Van Gelder, P., Hartmann, D., D'Hooge, R., De Strooper, B., Schymkowitz, J., and Rousseau, F. (2008) Lipids revert inert Abeta amyloid fibrils to neurotoxic protofibrils that affect learning in mice. *EMBO J.* **27**, 224–233
36. Hudson, S. A., Ecroyd, H., Kee, T. W., and Carver, J. A. (2009) The thioflavin T fluorescence assay for amyloid fibril detection can be biased by the presence of exogenous compounds. *FEBS J.* **276**, 5960–5972
37. Chen, S., and Wetzel, R. (2001) Solubilization and disaggregation of polyglutamine peptides. *Protein Sci.* **10**, 887–891
38. Pitiot, A. S., Santamaría, I., García-Suárez, O., Centeno, I., Astudillo, A., Rayón, C., and Balbín, M. (2007) A new type of NPM1 gene mutation in AML leading to a C-terminal truncated protein. *Leukemia* **21**, 1564–1566
39. Kim, C., Choi, J., Lee, S. J., Welsh, W. J., and Yoon, S. (2009) NetCSSP: web application for predicting chameleon sequences and amyloid fibril formation. *Nucleic Acids Res.* **37**, W469–W473
40. Silveira, J. R., Raymond, G. J., Hughson, A. G., Race, R. E., Sim, V. L., Hayes, S. F., and Caughey, B. (2005) The most infectious prion protein particles. *Nature* **437**, 257–261
41. Merlini, G., and Bellotti, V. (2003) Molecular mechanisms of amyloidosis. *N. Engl. J. Med.* **349**, 583–596
42. Rahimi, F., Shanmugam, A., and Bitan, G. (2008) Structure-function relationships of pre-fibrillar protein assemblies in Alzheimer's disease and related disorders. *Curr. Alzheimer Res.* **5**, 319–341
43. Cookson, M. R., and van der Brug, M. (2008) Cell systems and the toxic mechanism(s) of alpha-synuclein. *Exp. Neurol.* **209**, 5–11
44. Kourie, J. I. (2001) Mechanisms of prion-induced modifications in membrane transport properties: implications for signal transduction and neurotoxicity. *Chem. Biol. Interact.* **138**, 1–26
45. Demuro, A., Mina, E., Kayed, R., Milton, S. C., Parker, I., and Glabe, C. G. (2005) Calcium dysregulation and membrane disruption as a ubiquitous neurotoxic mechanism of soluble amyloid oligomers. *J. Biol. Chem.* **280**, 17294–17300
46. Eisenberg, D., and Jucker, M. (2012) The amyloid state of proteins in human diseases. *Cell* **148**, 1188–1203
47. Sawaya, M. R., Sambashivan, S., Nelson, R., Ivanova, M. I., Sievers, S. A., Apostol, M. I., Thompson, M. J., Balbirnie, M., Wiltzius, J. J., McFarlane, H. T., Madsen, A. O., Riekel, C., and Eisenberg, D. (2007) Atomic structures of amyloid cross-beta spines reveal varied steric zippers. *Nature* **447**, 453–457
48. Parrini, C., Taddei, N., Ramazzotti, M., Degl'Innocenti, D., Ramponi, G., Dobson, C. M., and Chiti, F. (2005) Glycine residues appear to be evolutionarily conserved for their ability to inhibit aggregation. *Structure* **13**, 1143–1151
49. Pawar, A. P., Dubay, K. F., Zurdo, J., Chiti, F., Vendruscolo, M., and Dobson C. M. (2005) Prediction of "aggregation-prone" and "aggregation susceptible" regions in proteins associated with neurodegenerative diseases. *J. Mol. Biol.*, **350**, 379–392
50. Batey, S., Randles, L. G., Steward, A., and Clarke, J. (2005) Cooperative folding in a multi-domain protein. *J. Mol. Biol.* **349**, 1045–1059
51. Ahmad, B., Vigliotta, I., Tatini, F., Campioni, S., Mannini, B., Winkelmann, J., Tiribilli, B., and Chiti, F. (2011) The induction of α-helical structure in partially unfolded HypF-N does not affect its aggregation propensity. *Protein Eng. Des. Sel.* **24**, 553–563
52. Falini, B., Martelli, M. P., Bolli, N., Sportoletti, P., Liso, A., Tiacci, E., and Haferlach, T. (2011) Acute myeloid leukemia with mutated nucleophosmin (NPM1): is it a distinct entity? *Blood* **117**, 1109–1120
53. Falini, B., Sportoletti, P., and Martelli, M. P. (2009) Acute myeloid leukemia with mutated NPM1: diagnosis, prognosis and therapeutic perspectives. *Curr. Opin. Oncol.* **21**, 573–581
54. Silva, J. L., De Moura Gallo, C. V., Costa, D. C., and Rangel, L. P. (2014) Prion-like aggregation of mutant p53 in cancer. *Trends Biochem. Sci.* **39**, 260–267

Received for publication December 30, 2014.
Accepted for publication May 1, 2015.